Controls on the seafloor exposure of detachment fault surfaces

Jean-Arthur Olive, Ross Parnell-Turner, Javier Escartin, Deborah K Smith, Sven E Petersen

Controls on the seafloor exposure of detachment fault surfaces

Jean-Arthur Olive[1]*, Ross Parnell-Turner[2,3], Javier Escartín[4], Deborah K. Smith[5], and Sven Petersen[6]

[1]Laboratoire de Géologie, Ecole Normale Supérieure / CNRS UMR 8538, PSL Research University, 24 rue Lhomond, 75005, Paris, France.
[2]Woods Hole Oceanographic Institution, 266 Woods Hole Rd., Woods Hole MA, 02543, USA.
[3]Now at: Scripps Institution of Oceanography, Institute of Geophysics and Planetary Physics, University of California, San Diego, La Jolla, CA 92093, USA
[4]Institut de Physique du Globe de Paris – CNRS UMR 7154, 1 rue Jussieu, 75005, Paris, France.
[5]National Science Foundation, 2415 Eisenhower Ave., Alexandria, VA, 22314, USA.
[6]GEOMAR / Helmholtz Centre for Ocean Research, Wischhofstrasse 1-3, 24148, Kiel, Germany.

*Corresponding author: olive@geologie.ens.fr

Keywords

Mid-ocean ridge; detachment faulting; oceanic core complex; critical taper; fault friction;

Highlights

- A small fraction of corrugated detachment fault surfaces is eventually exposed at the seafloor.
- Seafloor slopes indicate effective friction of ~0.2 on shallow part of detachments.
- Moderate-offset detachment faults may be largely blanketed by hanging wall material.
- Seafloor-shaping processes profoundly alter the morphology of oceanic core complexes.

Abstract

While oceanic detachment faults have been proposed to account for the accretion of ~40% of new seafloor in the North Atlantic ocean, clear exposures of large-offset, often-corrugated fault surfaces remain scarce and spatially limited. To help resolve this paradox, we examine the conditions under which detachment fault growth may or may not lead to extensive exposure of corrugated fault planes at the seafloor. Using high-resolution bathymetry from four detachment faults at the northern Mid-Atlantic Ridge, we investigate the rafting of hanging wall-derived debris over emerging fault scarps, which can lead to covering shallow-dipping corrugated fault surfaces. We model this process using critical taper theory, and infer low effective friction coefficients (~0.2) on the shallowest portion of detachment faults. A corollary to this result is that detachments emerging from the seafloor at angles <13º are more likely to become blanketed under an apron of hanging wall material. We generalize these findings as a simple model for the progressive exposure and flexural rotation of detachment footwalls, which accounts for the continued action of seafloor-shaping processes. Our model suggests that many moderate-offset, hidden detachment faults may exist along slow mid-ocean ridges, and do not feature an exposed fault surface.

1. Introduction

Bathymetric highs composed of mafic and ultramafic units are a characteristic feature of slowly accreted seafloor. These massifs are often capped by corrugated slip surfaces that represent the rotated footwalls of detachment faults with offsets on par with or greater than the thickness of young oceanic lithosphere (Cann et al., 1997; Tucholke et al., 1998; Parnell-Turner et al., 2018). These faults are generally found on ridge sections characterized by greater-than-average seismicity rates, lava geochemistry indicative of deeper fractionation, and hydrothermal activity (deMartin et al., 2007; McCaig et al., 2007; Escartín et al., 2008b; Blackman et al., 2011; Wilson et al., 2013; Olive and Escartín, 2016). Such observations led Escartín et al. (2008b) to postulate that detachment faulting enables a distinct mode of asymmetric seafloor spreading, favored wherever the magma supply of a mid-ocean ridge is subdued (Buck et al., 2005; Tucholke et al., 2008; Olive et al., 2010).

Significant portions of seafloor in the North Atlantic ocean are presently forming through asymmetric spreading (Escartín et al., 2008b; Cann et al., 2015). However, seafloor exposures of corrugated fault surfaces, a telltale sign of detachment fault growth (Cann et al., 1997), are often

spatially confined (≤ 10 km along-axis; Fig. 1) and only make up a small fraction of the > 40 km-long asymmetric sections of slow-spreading ridges. One explanation may be that detachment faults underlie entire ridge segments but are only exposed in areas where hanging wall rider blocks cannot develop (Smith et al., 2008; Reston and Ranero, 2011). Another is that detachment faults have a limited along-axis extent and connect with shorter-offset faults through complex relay structures (Smith et al., 2008; Tian and Choi, 2017). This debate warrants an improved understanding of how various seafloor-shaping processes modulate the exposure of pristine slip surfaces during detachment fault growth. These processes include gravitational mass wasting, which can both erode and cover portions of the footwall (Cannat et al., 2013), as well as rafting of hanging wall material onto the footwall. Here we investigate the mechanical and geometrical factors that lead to covering an emerging detachment surface under a hanging wall apron, making large-offset fault surfaces difficult to detect in shipboard bathymetric data. We then assess the relative impact of hanging wall rafting and mass wasting on the shape of oceanic detachment faults.

2. Seafloor morphology near oceanic detachment faults

Fig. 1 shows high-resolution (<2 m) bathymetry acquired using autonomous underwater vehicles at four detachment faults along the Northern Mid-Atlantic Ridge: 13º20'N (Escartín and Petersen, 2017; Escartín et al., 2017), 16º36'N and South Core Complex (SCC; Smith et al., 2014), and the Trans-Atlantic Geotraverse (TAG) detachment (Petersen et al., 2016). Geological interpretations of bathymetric features and textures, combined with in-situ observations at 13º20'N, suggest a common sequence of morphological domains at these detachments. The footwall cut-off scarp (i.e., the breakaway high marking the initial location of fault emergence) is often texturally rough (e.g., Fig. 1C), which is interpreted as the result of extensive gravitational mass wasting (Escartín et al., 2017). Towards the ridge axis, this chaotic terrain gradually transitions into the corrugated fault surface (Fig. 1A–D). This transition marks the place where angular blocks and talus stripped from the breakaway ridge no longer blanket freshly exposed corrugated fault surfaces. This difference is likely because the initially steep surface of growing detachments eventually rotates to gravitationally stable angles (<30º, Lavier et al., 1999), which are no longer prone to mass wasting (Cannat et al., 2013; Smith et al., 2014; Escartín et al., 2017).

The spatial extent of exposed corrugated surfaces varies greatly from one detachment to another. At the 13º20'N and SCC detachments, for example, the corrugated terrain exceeds 10 km^2

and abruptly connects with a rougher region termed "apron", axis-ward of the bathymetric moat that marks the fault termination or hanging wall cut-off (break in slope in Fig. 2). At 13º20'N the apron consists of basaltic and diabase blocks in an unlithified matrix, and incorporates some footwall-derived peridotite and gabbro (Escartín et al., 2017). The apron surface has a texture that is distinct from the adjacent volcanic terrain covering the ridge axis, and in many instances is thin enough for the underlying corrugations to be visible beneath (Fig. 1A–D; Fig. 3A). At TAG, the apron spans an area wider than the corrugated surface (Fig. 1A), and is directly adjacent to the chaotic terrain south of 26°09'N. This geometry suggests that the apron has the potential to blanket large extents of the detachment surface when certain geometrical and rheological conditions are met.

3. Detachment aprons as extensional Coulomb wedges

To understand how hanging wall material may be dragged onto the emerging fault surface, we model the apron as a cohesionless, critical Coulomb wedge of seafloor slope α with friction angle ϕ_0 (30º, appropriate for mafic lithologies) overlying a detachment fault of dip β and friction angle ϕ_D (Fig. 3A, Davis et al., 1983; Dahlen, 1984; Xiao et al., 1991; Yuan et al., 2015). We specifically use the critical wedge model of Yuan et al. (2015), which accounts for the possibility of fluid overpressure in the detachment. The fundamental assumption of wedge models is that the state of stress in the apron results from a balance between topographic and frictional forces and is on the verge of failure everywhere in critical wedges. The assumption of a cohesionless material is consistent with observations of the 13º20'N detachment suggesting that the apron consists of a mixture of unconsolidated rubble and finer-grained materials (Escartín et al., 2017).

We describe the state of stress within the wedge using two quantities ψ_D and ψ_0, which denote the angles between the most compressive principal stress (σ_1) and the detachment and apron surface, respectively. These are useful to determine potential slip lines within the apron, which are expected to lie at (±45°- ϕ_0/2) from σ_1 (Fig. 3A). By definition, the critical taper angle for the apron verifies:

$$\alpha + \beta = \psi_D - \psi_0 \ . \qquad (1)$$

If the entire apron is on the verge of Mohr-Coulomb failure, then only certain values of α, ψ_D and ψ_0 are admissible for a given β. These values verify the following set of implicit equations:

$$\frac{\sin\alpha'}{\sin\phi_0} - \sin\left(2\psi_0 + \alpha'\right) = 0 \ , \tag{2}$$

and

$$\sin\left(2\psi_D + \phi_D\right) - \frac{1-\lambda_D}{1-\lambda_0}\frac{\sin\phi_D}{\sin\phi_0} - \frac{\lambda_D - \lambda_0}{1-\lambda_0}\sin\phi_D \cos 2\psi_0 = 0 \ . \tag{3}$$

In equation (2), α' is defined as an angle verifying

$$\tan\alpha' = \frac{1-\rho_f/\rho}{1-\lambda_0}\tan\alpha \ , \tag{4}$$

where λ_0 and λ_D denote the fluid pressure ratio in the apron and detachment, respectively. The fluid pressure ratio is defined following Yuan et al. (2015) as

$$\lambda = -\frac{pf - \rho_f g D}{\sigma_z + \rho_f g D} \ , \tag{5}$$

with

$$\sigma_z = -\rho g z \cos\alpha - \rho_f g D \ . \tag{6}$$

In equations (5) and (6), p_f is fluid pressure at a point located at a seafloor-normal distance z beneath the apron surface (notation "D2" in Yuan et al., 2015). D is the water depth, and ρ and ρ_f refer to the density of the apron material (2400 kg m^{-3}) and of the fluid percolating within the apron (1000 kg m^{-3}). We assume that seawater easily percolates into the heavily damaged apron (Escartin et al., 2017), and exerts a hydrostatic fluid pressure throughout the wedge, i.e., fluid pressure increases downward in the wedge following a hydrostatic gradient. It can be shown that equation (5) reduces to $\lambda = \rho_f / \rho$ under hydrostatic conditions (see Appendix A. of Yuan et al. 2015). The fluid pressure ratio is thus set equal to 0.42 within the apron for the remainder of our study.

Equations (1-3) are formulated in terms of a residual function $F(\alpha, \psi_D, \psi_0) = 0$, and solved with a Newton method for a range of β-values. The associated Jacobian ∇F is estimated using centered finite difference with a step of 10^{-6} rad. Convergence is considered achieved when the norm of the residual falls below 10^{-11}. Our initial guess is $\alpha = \phi_0 / 2$, $\psi_0 = 20°$, and ψ_D set to either 20º or 120º, which are empirically found to promote convergence towards the upper or lower branch of the envelope, respectively. For a given pair of fault friction and fault fluid pressure values, the slope of the apron and the dip of the detachment must satisfy a set of equilibrium relations, plotted as stability envelopes in Fig. 3B. A MATLAB© script *GetWedgeEnvelope.m* is provided as part of the Supplementary Materials to generate stability envelopes (combinations of

α and β) as a function of ϕ_0, ϕ_D, λ_0, and λ_D. This function calls the subroutines *wedge_residual.m* (Residual function) and *wedge_jacobianFD.m* (Jacobian approximation), which are also provided.

Estimates for apron slope and detachment fault dip were obtained along 89 profiles oriented parallel to the spreading direction, crossing the hanging-wall cutoff (or moat; see Fig. 2 and 3A). High-resolution bathymetry was extracted along profiles spaced 100 m apart at the four study locations (Fig. 1). The position of the hanging-wall cutoff and spatial extent of the moat was identified in map-view, based upon the locus of change in bathymetric slope, and then used to define the hanging wall, footwall, and moat sections along each profile (Fig. 2). The mean apron slope was estimated for each profile using the slope of a linear least-squares fit to the bathymetry calculated over a 500 m distance downslope from the hanging wall-side edge of the moat, hence the moat itself is not included in the fit. The mean detachment fault dip was estimated using the slope of a linear fit to the bathymetry calculated 800 m upslope from the footwall-side edge of the moat. Uniform fitting lengths were chosen for consistency and to minimize the effects of local changes in slope, while not allowing profiles to extend onto the chaotic or neovolcanic terrains. The average apron slope across our detachments is 6.2±3.3º (1 standard deviation), and the average detachment dip right beneath the hanging wall cutoff is 13.8±2.5º.

4. Low effective friction on the shallow part of oceanic detachment faults

We follow a grid search approach to identify the product $\mu_D\,(1-\lambda_D) = \tan(\phi_D)(1-\lambda_D)$ that best explains the observed pair of (α, $\beta > -\alpha$) along 89 corrugation-parallel bathymetric transects at the four detachments shown in Figs. 1 and 2. For each pair (α, β), we construct 100 envelopes spanning values of $0.42 \leq \lambda_D \leq 0.82$ and $0 \leq \phi_D \leq 30$º. Each point on these envelopes corresponds to a specific stress orientation, which determines the orientation of possible slip lines (secondary faults) within the apron (Fig. 3A). We restrict our analysis to the upper branch of the envelopes, which predicts net extension in the wedge. We retain the envelopes whose upper branch lies at the shortest distance to each (α, β) pair, within an error of 2º (Fig. 3B). This set of best-fitting envelopes correspond to a narrow subset of (λ_D, ϕ_D) space, and consequently to a narrow range of $\mu_D\,(1-\lambda_D)$ values. We repeat this operation for an entire grid of (α, β) values, to which we are able to assign a best fitting $\mu_D\,(1-\lambda_D)$ with a typical error of ±0.01, plotted in Fig. 4 and as colored dots for each

profile in Fig. 1. For convenience, we also provide a polynomial approximation for $\mu_D(1-\lambda_D)$ as a function of (α, β), in degrees, which is accurate within the above error margin:

$$\mu_D(1-\lambda_D) = 0.008252 + 0.004973\beta - 0.003603\alpha + 0.00012\beta^2 + 1.026\times10^{-5}\alpha\beta + 7.116\times10^{-5}\alpha^2 - 1.853\times10^{-6}\beta^3 + 3.793\times10^{-7}\beta^2\alpha - 3.959\times10^{-6}\beta\alpha^2 - 2.385\times10^{-6}\alpha^3. \quad (7)$$

The inversion procedure described above yields a range of $\mu_D(1-\lambda_D)$ between 0.06 and 0.16, with a mode at 0.14 (Fig. 4). Since the geometry of the detachment surface is concave-down, measuring fault dip at the termination may underestimate the true dip of the detachment beneath the apron region (Fig. 3A). Estimates of the sub-seafloor fault geometry (available only for TAG and 13º20'N: deMartin et al., 2007; Parnell-Turner et al., 2017) suggest that detachments may steepen by at most ~10º across the apron (see section 5). Underestimating the average detachment dip beneath the apron by ~5º would lead to underestimating $\mu_D(1-\lambda_D)$ by ~0.04. Fig. 4 provides a straightforward way to assess the effect of an underestimated detachment dip (e.g., by translating the points towards the right by ~5º).

Profiles located away from the center of detachments tend to yield lower values of $\mu_D(1-\lambda_D)$ (Fig. 1), which may be due to the termination strike being highly oblique to the spreading direction at these locations owing to the three-dimensional fault morphology. By contrast, profiles oriented normal to the termination (i.e., most compatible with the two dimensional nature of the critical wedge model and often located in the central part of the detachment) commonly yield $\mu_D(1-\lambda_D)$ values ranging between 0.10 and 0.16, which we consider to be more reliable. Some short-wavelength apparent variability in our estimates directly reflects second-order tectonic features that offset the fault termination and alter slopes (e.g., at SCC, N and S of 16.425ºN, Fig. 1B). Our 2-D analysis is therefore unlikely to resolve frictional heterogeneities on a given detachment, if present.

Our estimates of $\mu_D(1-\lambda_D)$ can be translated into values of effective detachment friction, as defined by Dahlen (1984):

$$\mu_{eff} = \mu_D \frac{(1-\lambda_D)}{(1-\lambda_0)}. \quad (8)$$

This definition accounts for the buoyancy of fluids that percolate in the wedge. Under our assumption of hydrostatic fluid pressure in the apron (λ_0 = 0.42), we estimate effective friction coefficients between 0.17 and 0.28 in oceanic detachment faults. Low values of effective friction

are consistent with the common inference that the low strength of detachments enables their longevity (Escartín et al., 1997). Our strength estimates are however only representative of the uppermost ~1 km portion of detachments, which may be different from the rest of the fault. A possible manifestation of this difference could be the lack of shallow (≤ 3 km) microseismicity beneath TAG (deMartin et al., 2007) and 13º20'N (Parnell-Turner et al., 2017), as recorded by local ocean bottom seismometers (OBS) arrays. While very low effective friction on compressional décollements is typically attributed to elevated fluid pressure (e.g., Dahlen, 1984), such a scenario may be harder to envision in a tensional regime where cracks and pores are likely well connected. If fluid pressure is hydrostatic within the detachment fault zone, as was inferred by Hansen et al. 2013 for the Kane detachment down to depths of ~5 km, then the true friction coefficient of the fault material (μ_D) must lie between ~0.17 and ~0.26 (Fig. 3A). The precipitation of very weak minerals such as talc, with friction coefficients ranging between ~0.05 and 0.23 (Moore and Lockner, 2008; Escartín et al., 2008a) in the fault zone has been invoked as a key contributor to long-term strain localization (Escartín et al., 1997). By contrast, invoking moderately weak clay minerals (with friction coefficients of ~0.4, e.g., Tesei et al., 2012) to explain our estimates of effective friction would however require super-hydrostatic fluid pressure ratios between 0.6 and 0.75. The 13º20'N detachment, however, does not feature extensive weak phases (e.g., serpentinite, talc) and instead shows pervasive silicification (Bonnemains et al., 2017). The low effective friction of detachments may instead have a non-lithological origin. Episodes of seismic slip have been documented in the shallow, microseismically quiet portion of the 13º20'N detachment (Craig and Parnell-Turner, 2017). It is possible that infrequent earthquakes catastrophically reshape apron slopes to balance the low shear stresses that prevail during seismic rupture. The temporally-averaged apron slopes we measure may thus be influenced both by the long-term and the short-term fault strength, although this hypothesis is difficult to evaluate with the available data.

The above reasoning relies on the assumption that the apron wedge is critically stable, i.e., sits on the stability envelope as shown in Fig. 3B. At the 13º20'N detachment, small escarpments are visible in apron topography, potentially indicating secondary faulting (Fig. 3A). Internal wedge deformation alone would be indicative of the unstable wedge regime (outside of the stability envelope, Xiao et al., 1991). When coincident with slip on the detachment, secondary faulting implies a critically-stable apron at 13º20'N. However, slip on other detachments may occur without

faulting in the apron. Such systems would plot inside the stability envelope. Since increasing detachment friction shifts the stability boundary towards greater detachment dips (Hayman et al. 2003), one can identify the greatest value of detachment friction that allows a wedge of a given (α, β) to remain inside the stability envelope. This value corresponds to the critically-stable configuration. In other words, the effective friction determined with our approach must be thought of as an upper-bound on detachment strength.

5. Implications for the seafloor exposure of detachment fault surfaces

Regardless of the mechanistic interpretation for μ_{eff}, Coulomb wedge theory does predict an effective value for detachment friction that explains apron architecture (including the pattern of secondary faulting: Fig. 3A). A corollary to this model is that a detached piece of apron would not remain affixed to the footwall if the fault emerges from the seafloor with a slope greater than $\text{atan}(\mu_D (1 - \lambda_D)/(1 - \lambda_0)) \sim 13\pm3^\circ$ for $\mu_{eff} = 0.23\pm0.05$, because the low basal shear stresses would not be able to counteract gravity. Pieces of apron would thus slide back towards the hanging wall instead of blanketing the footwall. Conversely, a detachment fault emerging from the seafloor with a slope <13º should be extensively covered by hanging wall material.

The primary challenge in testing this idea is to infer detachment fault dip where it is not exposed. Such estimates are possible at TAG and 13º20'N, which constitute low and high end-members for the extent of the corrugated fault surface, respectively, and have both been instrumented with OBS arrays to illuminate the deeper portions of the fault zone through microseismicity (deMartin et al., 2007; Parnell-Turner et al., 2017). The clouds of extensional microseismicity observed at the roots of TAG and 13º20'N show dips as large as 70º at depths of ~7 km below seafloor. This clearly indicates an overall concave-down geometry of the detachment at depth. High-resolution seismic imaging studies will be needed to improve our knowledge of the near-surface geometry of these detachments. In the meantime, seafloor slopes reveal that a large portion of the apron domain at TAG is underlain by a detachment dipping with angles ≤10º (Fig. 2A), which is not the case at 13º20'N, where the fault emerges with slopes in excess of 15° (Fig. 2D). This simple comparison supports the idea that a gently dipping detachment is prone to extensive blanketing by apron material, and less likely to feature extensive, well exposed corrugated surfaces.

6. From covered to exposed detachment surfaces

Seafloor shaping processes are strongly sensitive to slope. Gravitational mass wasting is favored along slopes with an angle of repose steeper than ~20–30º (Cannat et al., 2013). By contrast, blanketing of exposed fault surfaces by hanging wall material is favored for shallow slopes <13º. The emerging slope of a detachment fault is known to change as the footwall undergoes flexural re-adjustment with continued slip (Buck, 1988; Lavier et al., 1999; Morris et al., 2009). Fig. 5 illustrates this process using an elastic model for footwall topography with increasing fault offset (Buck, 1988; Schouten et al., 2010; Olive and Behn, 2014). In the early stages of detachment growth, a breakaway ridge forms by slip along a high angle (>30º) fault, which triggers the extensive mass wasting that shapes the chaotic terrain (Fig. 5A). The morphology of young detachments may thus be strongly determined by the competition between the rate of footwall degradation by repeated rockslides, and the fault slip rate. Hence, efficient mass wasting could very well bury short-offset corrugated surfaces under footwall-derived debris.

As fault offset increases, flexural rotation decreases the emerging detachment slope until it becomes sub-horizontal (Fig. 5B). This stage favors extensive blanketing of the corrugated fault surface by hanging wall material, as seen today at TAG, a detachment fault with only ~5 km of offset (deMartin et al., 2007). Further extension on the detachment drives footwall doming (Fig. 5C), which increases the slope of the emerging footwall (>13º) and shrinks the apron domain, revealing an extensive corrugated surface (e.g., 13º20'N, with 9 km of offset). It should be noted that the emergence angle will to some extent also reflect the amount of volcanic material extruded onto the hanging wall (magmatic accretion in Fig. 5A).

Our model suggests that moderate-offset detachment faults may be widespread along slow-spreading ridges but remain undetected by shipboard bathymetric surveys, as they are largely blanketed by hanging wall material and do not (yet) expose large corrugated surfaces at the seafloor. Extensive high-resolution bathymetric surveys and a better mechanistic description of seafloor-shaping processes thus constitute crucial next steps to improve our understanding of slow-spreading ridge tectonics.

Acknowledgements

The authors wish to thank the ODEMAR (doi:10.17600/13030070) and M127 Science Parties as well as the teams operating the AUVs (WHOI's *Sentry* and GEOMAR's *Abyss*). JAO was funded

under NSF project EAR16500166. Cruise funding was provided through CNRS and IFREMER (JE), and GEOMAR and the EU-FP7-Project "Blue Mining: Breakthrough Solutions for the Sustainable Exploration and Extraction of Deep Sea Mineral Resources" under grant No. 604500 (SP). Xiaoping Yuan provided valuable guidance on the Coulomb wedge modeling. Finally, we thank Nadaya Cubas, Nicholas Hayman, and an anonymous reviewer for their thoughtful suggestions, which greatly improved our manuscript.

References

Blackman, D.K., et al., 2011, Drilling constraints on lithospheric accretion and evolution at Atlantis Massif, Mid-Atlantic Ridge 30ºN: J. Geophys. Res., v. 116, no. B07103, doi:10.1029/2010JB007931.

Bonnemains, D., Escartín, J., Mével, C., Andreani, M., and Verlaguet, A., 2017, Pervasive silicification and hanging wall overplating along the 13º20'N oceanic detachment fault (Mid-Atlantic Ridge): Geochem. Geophys. Geosyst., v. 18, no. 6, p. 2028–2053, doi:10.1002/2017GC006846.

Buck, W.R., 1988, Flexural Rotation of Normal Faults: Tectonics, v. 7, no. 5, p. 959–973, doi: 10.1029/TC007i005p00959.

Buck, W.R., Lavier, L., and Poliakov, A.N.B., 2005, Modes of faulting at mid-ocean ridges: Nature, v. 434, p. 719–723, doi: 10.1038/nature03358.

Cann, J.R., Blackman, D.K., Smith, D.K., McAllister, E., Janssen, B., Mello, S., Avgerinos, E., Pascoe, A.R., and Escartin, J., 1997, Corrugated slip surfaces formed at North Atlantic ridge-transform intersections: Nature, v. 385, p. 329–332.

Cann, J.R., Smith, D.K., Escartín, J., and Schouten, H., 2015, Tectonic evolution of 200 km of Mid-Atlantic Ridge over 10 million years — Interplay of volcanism and faulting: Geochem. Geophys. Geosyst., v. 16, p. 2303–2321, doi:10.1002/2015GC005797.

Cannat, M., Mangeney, A., Ondréas, H., Fouquet, Y., and Normand, A., 2013, High‐resolution

bathymetry reveals contrasting landslide activity shaping the walls of the Mid‐Atlantic Ridge axial valley: Geochem., Geophys., Geosyst., v. 14, no. 4, p. 996–1011, http://doi.org/10.1002/ggge.20056.

Craig, T.J., Parnell-Turner, R., 2017. Depth-varying seismogenesis on an oceanic detachment fault at 13°20'N on the Mid-Atlantic Ridge. Earth Planet. Sci. Lett., v. 479, p. 60–70, doi:10.1016/j.epsl.2017.09.020.

Collins, J.A., Smith, D.K., and Mcguire, J.J., 2012, Seismicity of the Atlantis Massif detachment fault, 30°N at the Mid-Atlantic Ridge: Geochem. Geophys. Geosyst., v. 13, no. 1, p. doi:10.1029/2012GC004210, doi: 10.1029/2012GC004210.

Dahlen, F.A., 1984, Noncohesive critical Coulomb wedges: An exact solution: J. Geophys. Res., v. 89, no. B12, p. 10,215–10,033.

Davis, D., Suppe, J., and Dahlen, F.A., 1983, Mechanics of fold-and-thrust belts and accretionary wedges: J. Geophys. Res., v. 88, no. B2, p. 1153–1172.

deMartin, B. J., Sohn, R.A., Canales, J.P., and Humphris, S.E., 2007, Kinematics and geometry of active detachment faulting beneath the Trans-Atlantic Geotraverse (TAG) hydrothermal field on the Mid-Atlantic Ridge: Geology, v. 35, p. 711–714, doi: 10.1130/G23718A.1.

Escartín, J., Hirth, G., and Evans, B., 1997, Effects of serpentinization on the lithospheric strength and the style of normal faulting at slow-spreading ridges: Earth Planet. Sci. Lett., v. 151, no. 3–4, p. 181–189, doi:10.1016/S0012-821X(97)81847-X.

Escartín, J., Andreani, M., Hirth, G., and Evans, B., 2008a, Relationships between the microstructural evolution and the rheology of talc at elevated pressures and temperatures: Earth Planet. Sci. Lett., v. 268, p. 463–475.

Escartín, J., Smith, D.K., Cann, J.R., Schouten, H., Langmuir, C.H., and Escrig, S., 2008b, Central role of detachment faults in accretion of slow-spreading oceanic lithosphere: Nature, v. 455,

355 no. 7214, p. 790–794, doi: 10.1038/nature07333.

356 Escartín, J., and Petersen, S., 2017, ODEMAR AUV Abyss (GEOMAR) + shipboard Pourquoi
357 Pas? Multibeam bathymetry – 13º20'N and 13º30'N Oceanic Core Complexes, Mid-Atlantic
358 Ridge: SEANOE, http://doi.org/10.17882/48335.

359 Escartín, J., Petersen, S., Bonnemains, D., Cannat, M., Andreani, M., Bezos, A., Chavagnac, V.,
360 Choi, Y., Godard, M., Haaga, K., Hamelin, C., Ildefonse, B., Jamieson, J., John, B., et al.,
361 2017, Tectonic structure, evolution, and the nature of oceanic core complexes and their
362 detachment fault zones (13°20' N and 13°30'N, Mid Atlantic Ridge): Geochem. Geophys.
363 Geosyst., 18, doi:10.1002/2016GC006775.

364 Hansen, L.N., Cheadle, M.J., John, B.E., Swapp, S.M., Dick, H.J.B., Tucholke, B.E., and Tivey,
365 M.A., 2013, Mylonitic deformation at the Kane oceanic core complex: Implications for the
366 rheological behavior of oceanic detachment faults: Geochem. Geophys. Geosyst., 14,
367 doi:10.1002/ggge.20184.

368 Hayman, N.W., Knott, J.R., Cowan, D.S., Nemser, E., and Sarna-Wojnicki, A.M., 2003,
369 Quaternary low-angle slip on detachment faults in Death Valley, California: Geology, v. 31,
370 no. 4, p. 343–346.

371 Lavier, L., Buck, W.R., and Poliakov, A., 1999, Self-consistent rolling-hinge model for the
372 evolution of large-onset low-angle normal faults: Geology, v. 27, no. 12, p. 1127–1130, doi:
373 10.1130/0091-7613(1999)027<1127:SCRHMF>2.3.CO;2.

374 McCaig, A.M., Cliff, R.A., Escartín, J., Fallick, A.E., and MacLeod, C.J., 2007, Oceanic
375 detachment faults focus very large volumes of black smoker fluids: Geology, v. 35, no. 10., p.
376 935–938.

377 Moore, D.E., and Lockner, D.A., 2008, Talc friction in the temperature range 25º–400ºC:
378 Relevance for fault-zone weakening: Tectonophysics, v. 449, p. 120-132,
379 doi:10.1016/j.tecto.2007.11.039.

380 Morris, A., Gee, J.S., Pressling, N., John, B.E., MacLeod, C.J., Grimes, C.B., and Searle, R.C.,

2009, Footwall rotation in an oceanic core complex quantified using reoriented Integrated Ocean Drilling Program core samples: Earth Planet. Sci. Lett., v. 287, no. 1–2, p. 217–228, doi: 10.1016/j.epsl.2009.08.007.

Olive, J.-A., Behn, M.D., and Tucholke, B.E., 2010, The structure of oceanic core complexes controlled by the depth-distribution of magma emplacement: Nat. Geosci., v. 3., p. 491–495, doi:10.1038/ngeo888.

Olive, J.-A., and Behn, M.D., 2014, Rapid rotation of normal faults due to flexural stresses: An explanation for the global distribution of normal fault dips: J. Geophys. Res., *119*, doi:10.1002/2013JB010512.

Olive, J.-A., and Escartín, J., 2016, Dependence of seismic coupling on normal fault style along the Northern Mid-Atlantic Ridge: Geochem. Geophys. Geosyst., 17, 4128–4152, doi:10.1002/2016GC006460

Parnell-Turner, R., Escartín, J., Olive, J.A., Smith, D.K., Petersen, S., 2018. Genesis of corrugated fault surfaces by strain localization recorded at oceanic detachments. Earth Planet. Sci. Lett. 498, 116–128. doi:10.1016/j.epsl.2018.06.034

Parnell-Turner, R., Sohn., R.A., Peirce, C., Reston, T.J., MacLeod, C.J., Searle, R.C., and Simão, N.M., 2017, Oceanic detachment faults generate compression in extension: Geology, doi:10.1130/G39232.1.

Petersen, S., and Shipboard Scientific Party, 2016, Cruise report M127 –Metal fluxes and Resource Potential at the Slow-spreading TAG Mid-ocean Ridge Segment (26°N, MAR)– Blue Mining@Sea: GEOMAR report 32, doi: 10.3289/GEOMAR_REP_NS_32_2016.

Reston, T.J., and Ranero C.R., 2011, The 3-D geometry of detachment faulting at mid-ocean ridges: Geochem. Geophys., Geosyst., v. 12, no. 7, doi:10.1029/2011GC003666.

410 Schouten, H., Smith, D.K., Cann, J.R., and Escartin, J., 2010, Tectonic versus magmatic extension
411 in the presence of core complexes at slow-spreading ridges from a visualization of faulted
412 seafloor topography: Geology, v. 38, no. 7, p. 615–618, doi: 10.1130/G30803.1.

413 Smith, D.K., Escartin, J., Schouten, H., and Cann, J.R., 2008, Fault rotation and core complex
414 formation: Significant processes in seafloor formation at slow-spreading mid-ocean ridges
415 (Mid-Atlantic Ridge, 13°–15°N): Geochem. Geophys. Geosyst., v. 9, no. 3, p.
416 doi:10.1029/2007GC001699, doi: 10.1029/2007GC001699.

417 Smith, D.K., Schouten, H., Dick, H.J.B., Cann, J.R., Salters, V., Marschall, H.R., Ji, F., Yoerger,
418 D., Sanfilippo, A., Parnell-Turner, R., Palmiotto, C., Zheleznov, A., Bai, H., Junkin, W., et al.,
419 2014, Development and evolution of detachment faulting along 50 km of the Mid-Atlantic
420 Ridge near 16.5°N: Geochem. Geophys. Geosyst., v. 15, p. 4692–4711,
421 doi:10.1002/2014GC005563.

422 Spencer, J.E., Reynolds, S.J., Scott, R.J., and Richard, S.M., 2016, Shortening in the upper plate
423 of the Buckskin-Rawhide extensional detachment fault, southwestern U.S., and implications
424 for stress conditions during extension: Tectonics, v. 35, no. 12, p. 3119–3136,
425 doi:10.1002/2016TC004345.

426 Tesei, T., Collettini, C., Carpenter, B.M., Viti, C., and Marone, C., 2012, Frictional strength and
427 healing behavior of phyllosilicate-rich faults: J. Geophys. Res., v. 117,
428 doi:10.1029/2012JB009204.

429 Tian, X., and Choi, E., 2017, Effects of axially variable diking rates on faulting at slow spreading
430 mid-ocean ridges: Earth Planet. Sci. Lett., v. 458, p. 14–21.

431 Tucholke, B.E., Lin, J., and Kleinrock, M.C., 1998, Megamullions and mullion structure defining
432 oceanic metamorphic core complexes on the Mid-Atlantic Ridge: J. Geophys. Res., v. 103, no.
433 B5, p. 9857–9866.

434 Xiao, H.-B., Dahlen, F.A., and Suppe, J., 1991, Mechanics of extensional wedges: J. Geophys.
435 Res., v. 96, no. B6, p. 301–318.

436 Wilson, S.C., Murton, B.J., and Taylor, R.N., 2013, Mantle composition controls the development
437 of an Oceanic Core Complex: Geochem. Geophys. Geosyst., v. 14., no. 4, doi:
438 10.1002/ggge.20046

439 Yuan, X.P., Leroy, Y.M., and Maillot, B., 2015, Tectonic and gravity extensional collapses in
440 overpressured cohesive and frictional wedges: J. Geophys. Res., v. 120,
441 doi:10.1002/2014JB011612.

442

Figure captions

Figure 1. A–D: Seafloor terrain and slopes at four Mid-Atlantic Ridge detachment faults (locations shown in inset E), from AUV bathymetric data gridded at 2 m resolution and plotted at equal scale. Colored dots mark detachment termination, color-coded by $\mu_D(1-\lambda_D)$ (see section 4). Red arrows indicate spreading direction, pointing away from the ridge axis. Dashed lines show northernmost and southernmost spreading-parallel profiles bracketing topographic profiles used here, which are evenly spaced at 100 m. RR = rubble ridges, i.e., small fragments of broken-down apron carried by the fault surface.

Figure 2. High-resolution bathymetric profiles oriented parallel to the transport direction (inferred from corrugations), spaced 100 m apart between dashed lines in Fig. 1. Thin red/blue/black sections are hanging wall / footwall / moat sections of each profile, respectively; thick gray lines are linear fits used to obtain estimates for apron slope and detachment fault dip. A: TAG; B: 16°36'N OCC; C: South Core Complex; D: 13°20'N OCC.

Figure 3. A: Schematic cross section of the termination of the 13º20'N detachment fault, based on topographic profile XX' from Fig. 1D. Inset shows a zoom on the hanging wall apron, with inferred slip line orientations. Setup of corresponding critical taper model shown below. B: Stability envelopes calculated using extensional taper model. These envelopes all account for slope of 13º20'N apron measured along crest profile, and all correspond to a specific range of $\mu_D(1-\lambda_D)$ values = 0.15±0.01 on the detachment fault.

Figure 4. Contours of best-fitting values of $\mu_D(1-\lambda_D)$ on a detachment fault of dip β underlying an apron of slope α, assuming a critical taper model with hydrostatic fluid pressure and an internal friction angle of 30º. Symbols indicate measured slopes along the profiles bracketed in Fig. 1. hc: hanging wall cutoff (termination).

Figure 5. Progressive rollover and exhumation of a detachment fault. Blue curve is rolling hinge model of Buck (1988) for an elastic plate of flexural wavelength L (~1 km at the MAR, Schouten et al., 2010). A: At moderate offsets (e.g., fault heave = $2L$), footwall slopes are steep, which leads

to mass wasting of the breakaway (fc: footwall cutoff) region, eventually forming the chaotic terrain. B: At intermediate offsets (e.g., fault heave = 3*L*) flexural rotation of the footwall leads to very shallow seafloor slopes, promoting a widespread apron zone burying most of the detachment surface. C: Finally, at large offsets (e.g., fault heave = 4*L*) late-stage doming occurs close to the fault termination (hc: hanging wall cutoff) where seafloor slopes increase, reducing the extent of the apron and exposing the corrugated detachment surface (wiggly lines).

Figure 1

Click here to download Figure: Figure_1_OCC_maps_SMALL.pdf

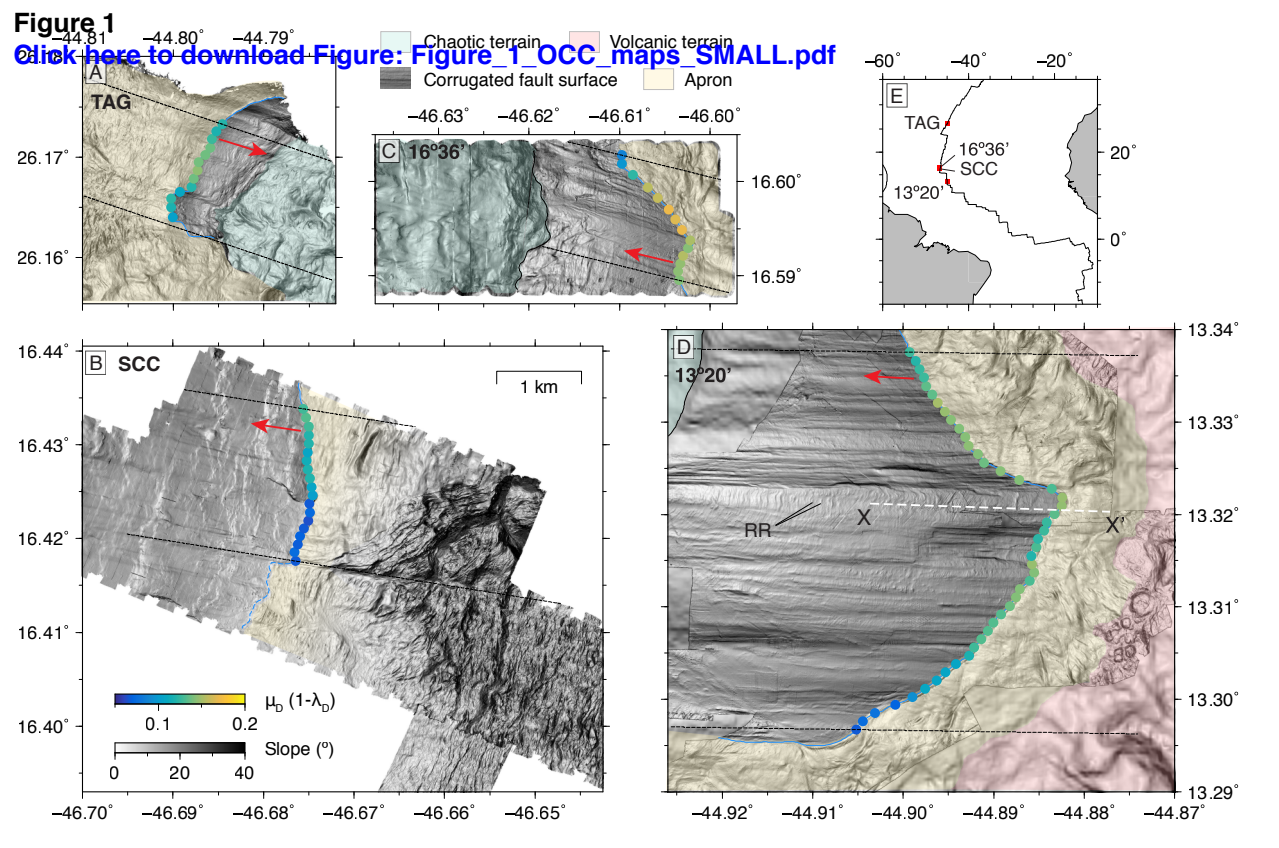

Figure 2

Click here to download Figure: Figure_2_all_slopes.pdf

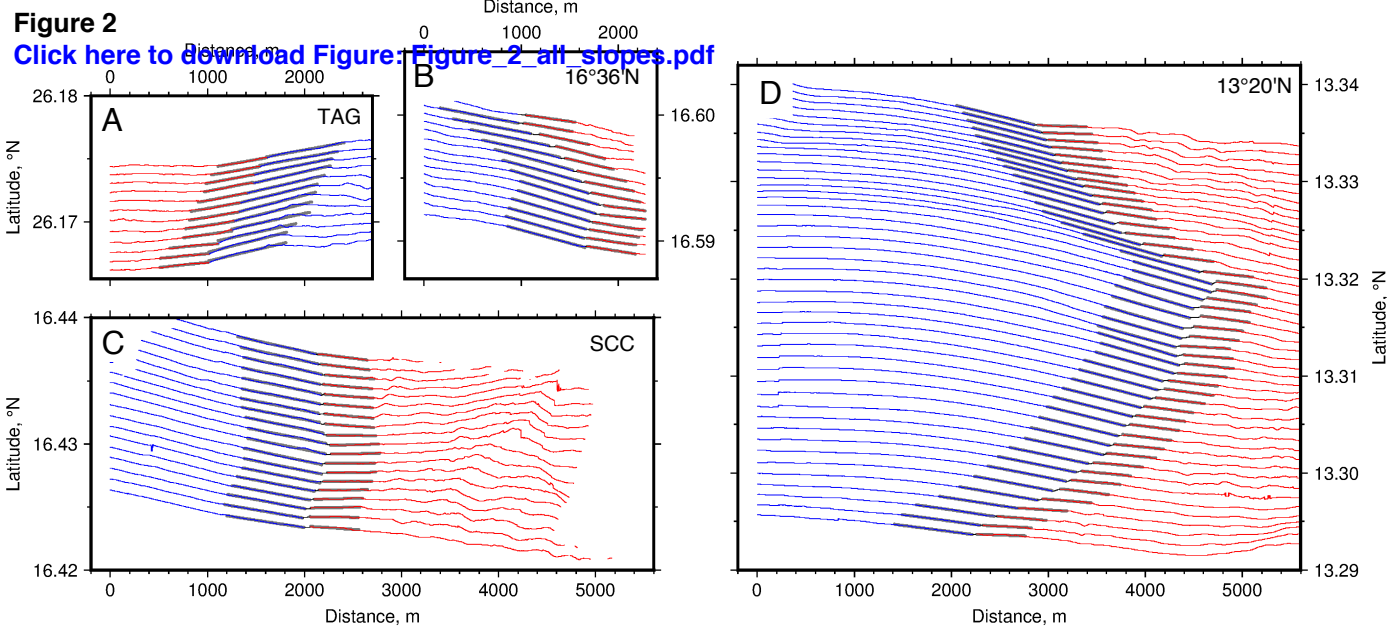

Figure 3
Click here to download Figure: Figure_3_apron_model.pdf

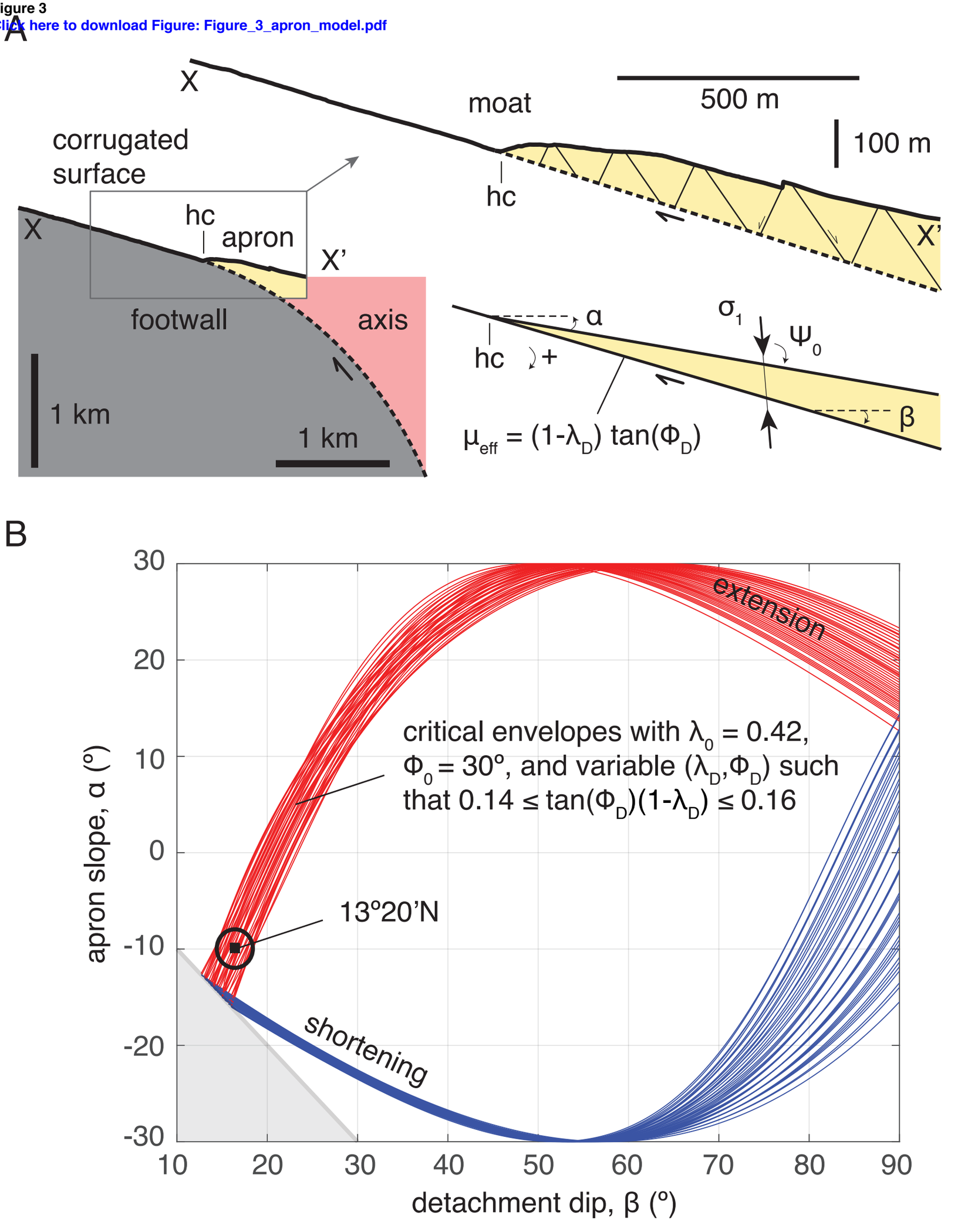

Figure 4

Click here to download Figure: Figure_4_slopes2friction.pdf

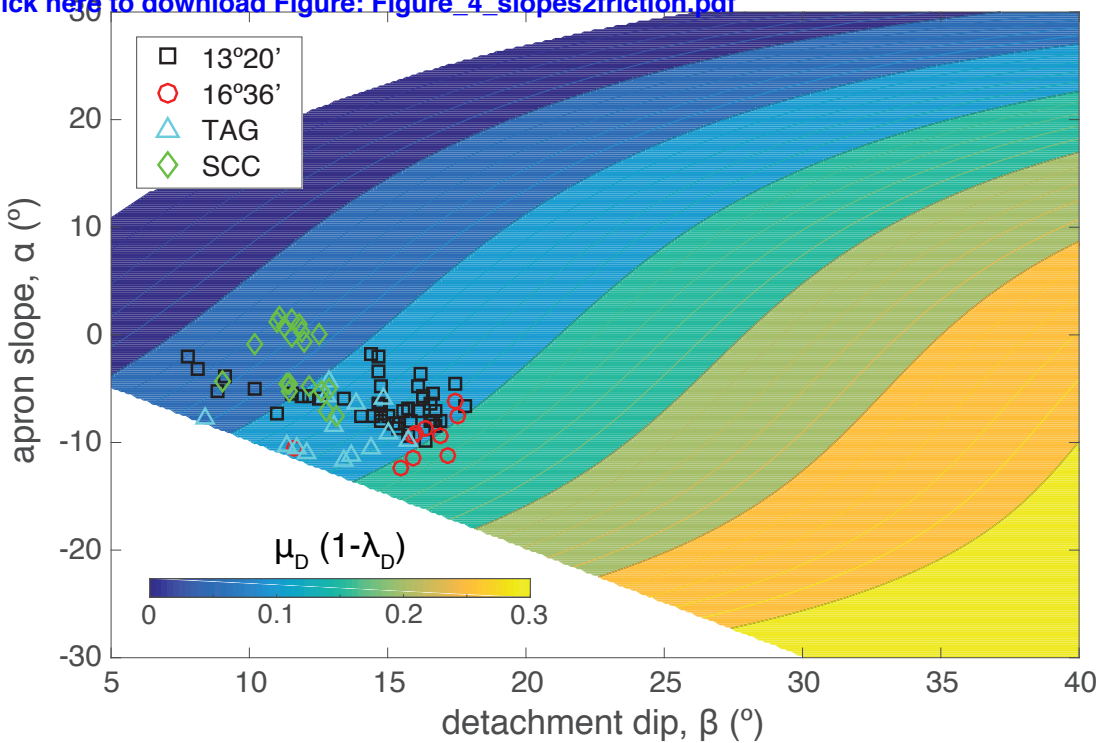

Figure 5

Click here to download Figure: Figure_5_synthetic_cartoon.pdf